Low temperature synthesis of stable γ–$CsPbI_3$ perovskite layers for solar cells obtained by high throughput experimentation

Pascal Becker[1,2], José A. Márquez[1], Justus Just[1,3], Amran Al-Ashouri[4], Charles Hages[1], Hannes Hempel[1], Marko Jošt[4], Steve Albrecht[4], Ronald Frahm[2] and Thomas Unold[1*]*

[1]Helmholtz-Zentrum-Berlin, Hahn-Meitner-Platz 1, 14109 Berlin, Germany
[2]Bergische Universitaet Wuppertal, Gausstrasse 20, 42119 Wuppertal, Germany
[3]Lund University, Paradisgatan 2, 22100 Lund, Sweden
[4]Young Investigator Group Perovskite Tandem Solar Cells, Helmholtz-Zentrum-Berlin, Hahn Meitner-Platz 1, 14109 Berlin, Germany

Keywords: inorganic halide perovskites, thin film solar cell, optoelectronics, coevaporation, high throughput characterization

Abstract

The structural phases and optoelectronic properties of co-evaporated $CsPbI_3$ thin films with a wide range of [CsI]/[PbI_2] compositional ratios are investigated using high throughput experimentation and gradient samples. It is found that for CsI-rich growth conditions, $CsPbI_3$ can be synthesized directly at low temperature into the distorted perovskite γ– $CsPbI_3$ phase without detectable secondary phases. In contrast, PbI_2-rich growth conditions are found to lead to the non-perovskite δ-phase. Photoluminescence spectroscopy and optical pump-THz probe mapping show carrier lifetimes larger than 75 ns and charge carrier (sum) mobilities larger than 60 cm^2/Vs for the γ-phase, indicating their suitability for high efficiency solar cells. The dependence of the carrier mobilities and luminescence peak energy on the Cs-content in the films indicates the presence of Schottky defect pairs, which may cause the stabilization of the γ–phase. Building on these results p-i-n type solar cells with a maximum efficiency exceeding 12 % and high shelf stability of more than 1200 h are demonstrated, which in the future could still be significantly improved judging on their bulk optoelectronic properties.

1. Introduction

After the steep rise of hybrid organic-inorganic perovskite solar cells (PSCs) with certified power conversion efficiencies over 23 %,[1,2] fully inorganic PSCs with cesium replacing the organic cation have lately drawn significant attention due to their better thermal stability.[3,4] In particular, lead-based $CsPbX_3$ (X = I, Br) represents a promising candidate for high efficiency stable photovoltaic devices. While the band gap of $CsPbBr_3$ is about 2.3 eV[5,6] and therefore too large for photovoltaic applications,[3] the band gap of $CsPbI_3$ of 1.76 eV is ideal for top cells in tandem applications in conjunction with low band gap bottom cells.[7] Solution processed thin films based on $CsPbI_3$ absorber layers recently have reached an efficiency of 17 %,[8] while the current world record for quantum dot solar cells employing $CsPbI_3$ nanocrystals was reported with efficiencies exceeding 13%.[9]

For $CsMI_3$ (M = Pb, Sn), four phases are expected: the cubic (α), the tetragonal (β), and two orthorhombic phases (a black γ and a non-perovskite yellow δ-phase). Unfortunately, at room temperature the orthorhombic δ-phase with a band gap of 2.8 eV is thermodynamically favored over the desirable cubic perovskite α- and tetragonal-β and orthorhombic-γ perovskite phases.[10,11] Thus at room temperature the material has the tendency to either form directly in the δ-phase or to undergo a spontaneous phase change into the δ-phase, making it difficult to obtain or retain $CsPbI_3$ films in the perovskite phase.[10] The identification of the room-temperature phase has been a matter of considerable debate, with a number of earlier literature reports suggesting the (metastable) presence of the cubic-α phase [12–14]. However, more recent reports demonstrated that the α-phase is only stable at high temperatures above 310 °C[10,15] and undergoes a phase transition into the β- and γ-phases when the samples are cooled down to ambient temperatures. In order to add clarity to this issue, special attention will be placed on the characterization of the crystal structure that $CsPbI_3$ adopts in this work. In order to obtain $CsPbI_3$ in the perovskite phase thin films are

usually heated above 320 °C to convert the yellow δ-phase into the perovskite phase.[14,16–19] However, such high temperatures can damage organic charge transport layers or flexible substrates, which limits the application in p-i-n solar cell architectures and in tandem devices. Different approaches have been used to form and stabilize the perovskite phase of $CsPbI_3$ at lower temperature, for example the use of mixed halide perovskites with partial substitution of iodide by bromide ($CsPbI_{3-x}Br_x$),[20–24] or the introduction of bismuth,[12] strontium,[25] sulfobetaine zwitterions[26], hydroiodic acid,[27,28],34 and of phenethylamine (PEA).[28–30] Although it has been suggested that small grain sizes may aid in the stabilization of the γ-phase at room temperature, the microscopic origin and growth conditions necessary to obtain a γ-phase at room temperature are still unclear.

In this work we show a direct route to synthesize $CsPbI_3$ in the distorted perovskite γ-phase by co-evaporation of CsI and PbI_2 at a substrate temperature of 50 °C without the need for a post-deposition annealing treatment. Our process results in thin films with a lateral gradient in composition which allows us to study in depth the composition-dependent structural and optoelectronic properties of this material system. To this end, contactless high throughput characterization including time-resolved and calibrated absolute photoluminescence (PL) and optical pump THz probe (OPTP) spectroscopy is employed. Finally p-i-n-type solar cells were fabricated using the low temperature-deposited $CsPbI_3$ thus demonstrating the applicability of the deposition route presented here for devices manufacturing.

2. Results and Discussion

2.1. Structure, composition and chemical stability of the γ-$CsPbI_3$ phase.

To evaluate the influence of the compositional deviations from stoichiometry of $CsPbI_3$ on the materials properties, thin-films were deposited by co-evaporation of CsI and PbI_2 on quartz glass at a substrate temperature of 50 °C as shown in ***Figure 1a***.

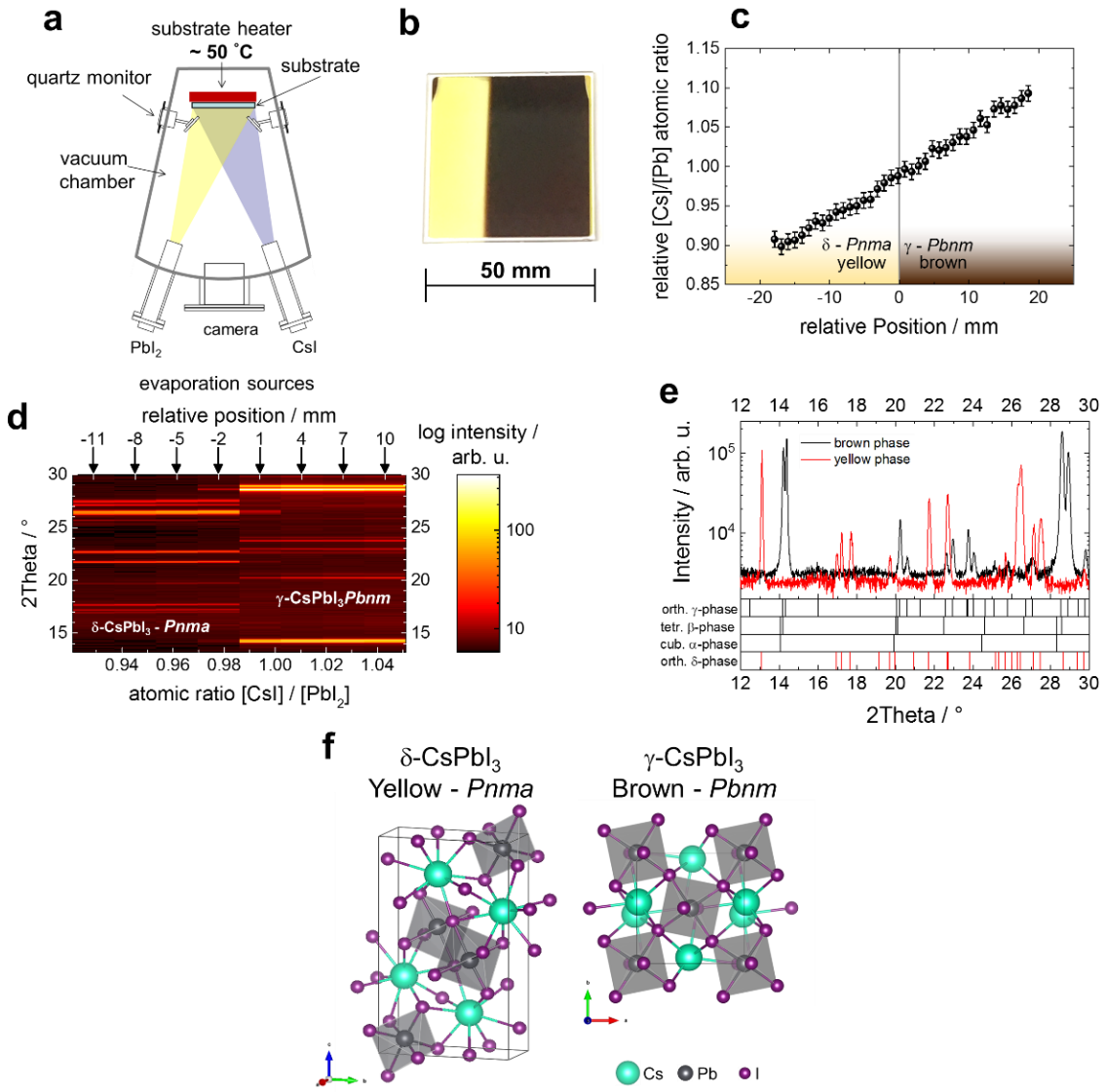

Figure 1. (a) Schematics of the evaporation chamber used in this work. **(b)** Photographic image of an as-evaporated $CsPbI_3$ film. Two clearly distinct regions can be observed; one yellow, one brown. **(c)** [Cs]/[Pb] atomic ratio from XRF measurement as a function of position measured perpendicular to the phase boundary. The yellow and brown phases are color-labelled in the background **(d)** XRD patterns from a line scan for the combinatorial sample showing the phase transition as a function of composition (sample position). The arrows mark the positions at which measurements are taken. **(e)** XRD patterns acquired in the brown and yellow regions of the sample. **(f)** Unit cells of the δ-$CsPbI_3$ (yellow – Pnma) and the γ-$CsPbI_3$ (brown – Pbnm) phases.

The substrate is not rotated during deposition to allow the formation of a compositional gradient across the sample and the evaporation rates of both sources were controlled individually with quartz balance monitors. ***Figure 1b*** shows a photographic image of the as-evaporated sample where two clearly distinct regions can be observed, indicating the presence of a brown and a yellow phase with a distinct phase boundary. The chemical composition of the sample was analyzed by X-ray fluorescence (XRF) mapping. **Figure 1*c*** shows a line-scan perpendicular to the yellow-to-brown phase boundary. A monotonic, almost linear increase of the relative [Cs]/[Pb]-atomic ratio is observed moving from the yellow to the brown region of the sample, with a variation of the [Cs]/[Pb]-atomic ratio of more than 20 % across the 50 mm wide substrate. Interestingly, a stoichiometric 1:1:3 composition is observed directly at the phase boundary between the yellow and brown phase, although we note that the absolute uncertainty in the [Cs]/[Pb]-atomic ratio is estimated to be about 10 %.

To identify the structural properties of the sample as a function of composition an X-ray diffraction (XRD) line-scan was performed in direction of the chemical gradient. **Figure 1*d*** shows XRD patterns acquired as a function of sample position relative to the boundary between the two regions. Again a sharp boundary with distinctly different XRD patterns is observed between the yellow and brown regions of the sample within the experimental resolution. Typical diffractograms for the yellow and brown phase, respectively, are shown in **Figure 1*e***. Comparison with reference peak positions shows that the observed phases can only be assigned to the distorted perovskite γ-$CsPbI_3$ (space group *Pbnm*) in the brown region and the non-perovskite phase δ-$CsPbI_3$ (space group *Pnma*) in the yellow region.[10] This confirms that the stable perovskite at room temperature is the γ–$CsPbI_3$ and not the cubic α phase, in agreement with some recent studies.[10,15,31,32] Le Bail analysis was performed for the patterns acquired in the laboratory for both phases taking as starting models the δ and γ

phases reported by Marronnier et al.[10] The analysis resulted in the δ-phase with lattice parameters a = 10.471 ± 0.002 Å, b = 4.790 ± 0.001 Å and c = 17.781 ± 0.003 Å, and the γ-phase with a = 8.629 ± 0.001 Å, b = 8.834 ± 0.001Å and c = 12.472 ± 0.002 Å (see ***Figure S1*** and ***Table S1***). We note that the lattice parameters values obtained for the γ-phase differ from the previously reported ones in the literature for the γ-phase.[10,31,32] In particular, we observe that the ratio of the lattice parameters of the unit cells vary between the four studies. We estimate that our sample has the largest ratio in a / b and the smallest in $c / (a+b)$ in comparison with the values reported in literature including $CsPbI_3$ nanocrystals (see ***Table S1)***. The variations on the unit cell parameters might affect the phase stability and the octahedral distortion, therefore also affecting the optoelectronic properties of the material. Such differences in the lattice parameters might be caused by different synthesis methods, composition and different thermal history of the sample and further studies are required to fully understand their correlation. Importantly, our work demonstrates that pure $CsPbI_3$ can be directly synthesized in a perovskite phase at low temperatures < 60 °C in CsI-rich conditions without the need of a post-deposition annealing treatment which is in contrast to many previous reports.[3,17,33] It is important to note that despite the non-stoichiometric composition in most parts of the sample, the XRD linescan shown in ***Figure 1d*** does not indicate the presence of secondary phases, e.g. CsI, PbI_2 or Cs_2PbI_4 for the compositional regime 0.96 ± 0.1 < [CsI]/[PbI_2] 1.07 ± 0.1. For larger stoichiometric variations we observe the appearance of a broad low intensity feature in the diffraction patterns that we tentatively attribute to PbI_2 for [CsI]/[PbI_2] < 0.96 ± 0.1 and CsI for [CsI]/[PbI_2] > 1.07 ± 0.1 (see supplementary material ***Figures S2*** and ***S3***) .

To confirm that the position of the phase boundary is directly related to the chemical composition of [CsI]/[PbI_2] = 1 and not due to other specific experimental conditions, three combinatorial samples were prepared for which the ratio of the evaporation rate of CsI and

PbI_2 was varied, which should lead to a spatial shift of the phase boundary. For each sample, the yellow to brown phase boundary was found at a different sample position. However, the composition at the phase boundary was identical (see ***Figure S4***). This corroborates that using low temperature processing the brown phase can only be obtained for $[CsI]/[PbI_2] \geq 1$.

In our measurements we do not observe the presence of secondary phases for a significantly wide range of compositions around the point of stoichiometry. This indicates the presence of Schottky-type defect pairs in the perovskite structure, which can be described by the chemical formula $Cs_{1+x}Pb_{1-x}I_{3-x}$. However, we note that this cannot unambiguously concluded taking the detection limits of the measurement and the low expected concentration of CsI into account (see figure S3) although futher evidence is provided by the optoelectronic analysis described below. The formation of Schottky defect pairs such as [V_{Pb}^{-2} and $2V_I^{+1}$] has been theoretically predicted to have a low formation energy and thus to be thermodynamically favored.[34] Experimentally this has been shown in hybrid perovskites with the incorporation of di-cationic molecules increasing the stability of the phase in so called "hollow" perovskites.[35] The term "hollow" perovskite arises from the abundance of lead and iodine vacancies in the $[PbI_3]$ framework.[35] Starting from $CsPbI_3$, the concentration of these Schottky-defects is expected to increase as x increases and the $Cs_{1+x}Pb_{1-x}I_{3-x}$ phase becomes more CsI rich, which might increase the stability of the perovskite phase in a similar way to what it has been observed in hybrid-hollow perovskites.[35] Alternatively it has been proposed that the stabilization of γ–$CsPbI_3$ is favored over δ–$CsPbI_3$ by a decreasing grain sizes (or enlarged grain boundary surface area), due to the lower surface energy of the former, compared to the latter phase.[36] In a recent study γ–$CsPbI_3$ has been synthesized by annealing at 100 °C for average grain sizes between 100 nm and 200 nm, where the small grain sizes were obtained by using addition of HI and H_2O in the solution process.[36] In the current work small grain sizes between 100 nm and 200 nm are obtained without any additives in the CsI

rich region during the evaporation process. On the other hand, somewhat larger grain sizes are observed for the region of the sample crystallizing in the δ–$CsPbI_3$ phase. This could also explain the stabilization of the γ–phase caused by an inhibition of grain growth for samples grown under CsI-excess in the hollow-perovskite region.

2.2 Dependence of the optoelectronic properties on composition.

The $CsPbI_3$ γ-brown phase shows a sharp absorption onset at about 1.76 eV with absorption coefficient values exceeding $3x10^4$ cm^{-1} as shown for $[CsI]/[PbI_2] \approx 1.10$ in ***Figure 2a*** together with a photoluminescence (PL) spectrum acquired under one sun equivalent conditions (see also ***Figure S5)***. It can be seen that the emission is centered at the energy of the absorption onset, indicating that the observed emission band originates from a band-band transition. To investigate the change of the optical properties as a function of CsI/PbI_2 ratio, the PL peak position is plotted as a function of composition in the top graph of ***Figure 2d***. A small blue-shift of the energy of the PL band (PL_{max}) is observed with increasing CsI/PbI_2 ratio in the brown phase. A similar trend is observed in the external PL quantum yield (EQE_{PL}), which increases from $3x10^{-4}$ % for $[CsI]/[PbI_2] \approx 1.0$ to $1x10^{-2}$ % for $[CsI]/[PbI_2] \approx 1.10$ indicating that non-radiative recombination is significantly reduced as the $CsPbI_3$ phase becomes more CsI-rich. This is further confirmed by a similar trend observed in the minority carrier lifetime (τ_{SRH}) derived from the TRPL decays shown in ***Figure 2b***, which shows low values $\tau_{SRH} < 10$ ns close to the phase boundary and increases up to a maximum values close to 80 ns $[CsI]/[PbI_2] \approx 1.05$. Interestingly, both the EQE_{PL} and the carrier lifetime τ_{SRH} start to decrease again, when the $[CsI]/[PbI_2]$ ratio is increased beyond about 1.05 which is also close to composition when a CsI-segregation becomes detectable. Optical Pump THz Probe (OPTP) measurements allow to characterize the charge carrier dynamics with high temporal resolution,[37] in particular the identification of fast carrier trapping processes in the

photoconductivity decays, and the estimation of intra-grain carrier mobilities form their complex frequency response.[38] An overview of such measurements for the sample consisting of the yellow and the brown phase is shown in Figure 2c, where the photoconductivity decay is plotted as a function of the sample position. It can be seen that for the yellow region no photoconductivity response is observed, although the samples where excited with fs-pulses above the band gap of the yellow phase. On the other hand in the γ–$CsPbI_3$ region, decay times compatible with the TRPL decays are detected, although decreasing strongly close to the phase boundary (see also SI). Interestingly, the transients do not exhibit any fast decay component within the first picoseconds, which indicates that charge carrier trapping plays a minor role in the recombination kinetics here.

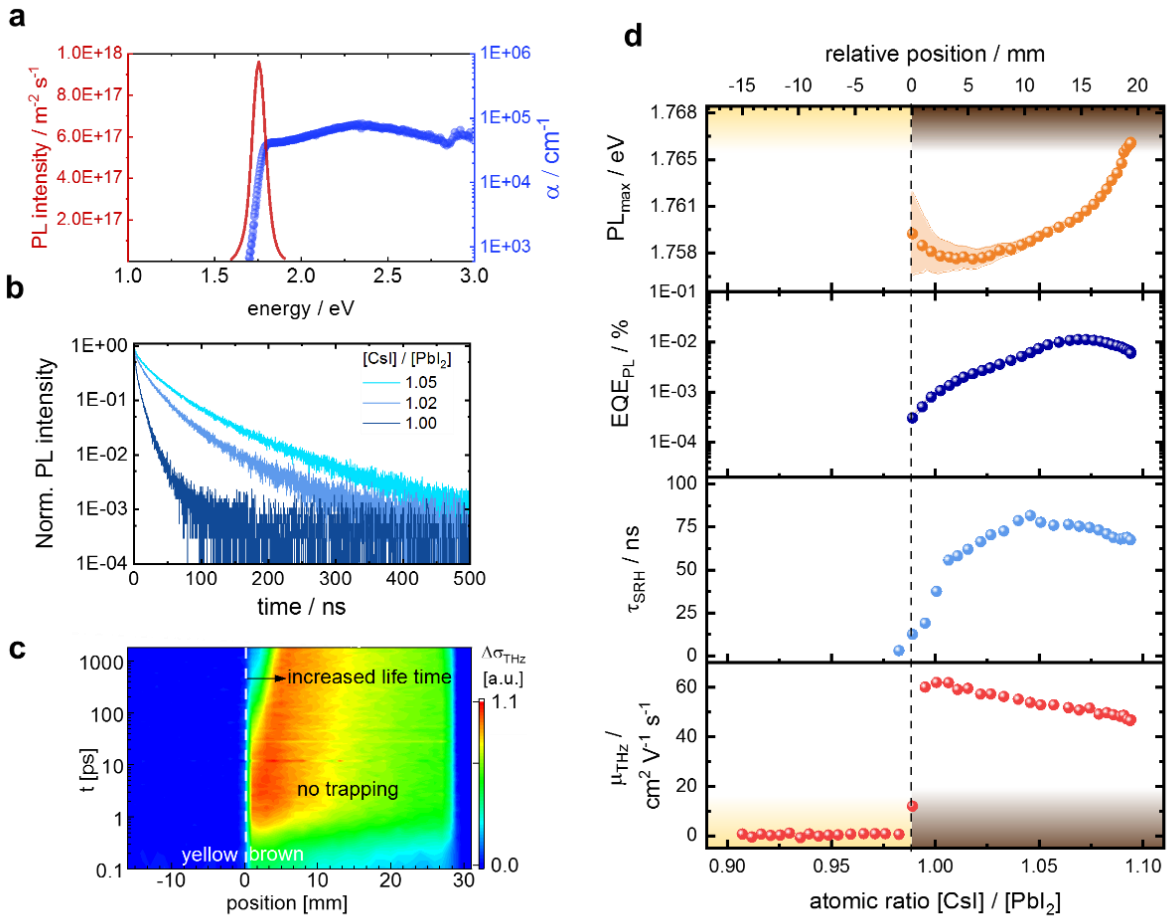

Figure 2. (a) Absolute intensity PL spectrum and absorption coefficient for $[CsI]/[PbI_2] \approx 1.10$, **(b)** TRPL decays as a function of $[CsI]/[PbI_2]$ ratio. **(c)** THz photoconductivity transient map collected at different positions of the sample with different $[CsI]/[PbI_2]$ ratios. **(d)** Optoelectronic properties determined from the aforementioned measurements as a function of $[CsI]/[PbI_2]$ atomic ratio and relative position on the sample. From top to bottom: Photon energy of the PL maximum (PL_{max}) and external PL quantum yield (EQE_{PL}) extracted from the hyperspectral PL imaging data, minority carrier lifetime (τ_{SRH}) deduced from TRPL and sum mobility (μ_{THz}) deduced from terahertz spectroscopy.

The sum of electron and hole mobility, μ_{THz}, extracted from the spectral response of the OPTP measurements are shown in ***Figure 2d*** as a function of the composition on the sample. It can be seen that for the yellow δ-phase, the μ_{THz} values are < 0.1 $cm^2V^{-1}s^{-1}$ proving the unsuitability of the yellow phase as a photovoltaic material. On the other hand, large carrier mobilities > 65 $cm^2V^{-1}s^{-1}$ are observed for the brown region (γ-phase) of the sample, which continuously decrease to about 45 $cm^2V^{-1}s^{-1}$ for increasing $[CsI]/[PbI_2]$. We note that the mobilities observed for the γ-phase in the present study are similar or higher than the values previously reported for solution processed $CsPbI_3$ films with a post annealing treatment and for $CH_3NH_3PbI_3$ (MAPI).[17,39,40]

Interestingly, opposite to the trend in the carrier lifetime and EQE_{PL}, the carrier mobilities almost immediately decrease as the sample becomes more Cs-rich. This observation may be further evidence (together with the change in luminescence peak energy shown in figure 2d) for the presence of the Schottky-type defect pairs discussed above, which would lead to a decreasing electronic connectivity of its $[PbI_6]$ octahedra building blocks with increasing Cs-content. Whereas in stoichiometric $CsPbI_3$ in the α, β and γ-phase,[10] each of the $[PbI_6]$ octahedra share their corners with another octahedron leading to extended wavefunctions of the valence band (halogen *p* orbitals and Pb-*s*-orbitals) and the conduction band (unoccupied Pb-*p* orbitals), this octahedra interconnectivity becomes disrupted for Cs-excess in the so-

called hollow perovskites.[41] Thus for increasing Cs-content a reduction in the carrier mobilities is predicted from theory[42] and indeed observed in our experiments. In the δ-phase the [PbI_6] octahedra are present in a non-corner-sharing double-chain, resulting in lower crystallographic dimensionality as well as a less dispersive and thus higher effective mass CBM and VBM[41,42] (see ***Figure 1f***). These properties predict very poor charge carrier mobilities, which again are confirmed in our experiments. The low values of μ_{THz}, the bandgap value of 2.8 eV,[43] and lack of measurable carrier lifetime for this non-perovskite phase, show that this polymorph is not suitable for photovoltaic applications as described by previous reports.[44]

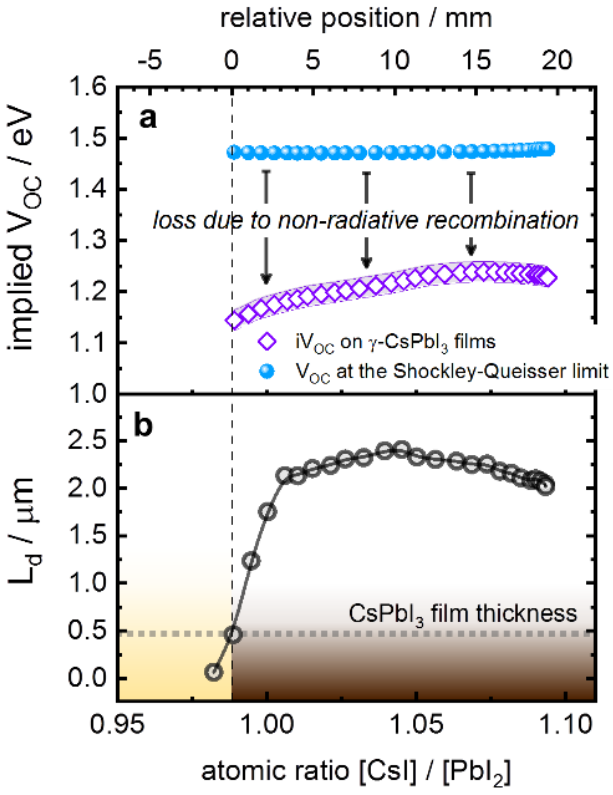

Figure 3 (a) Implied V_{oc} calculated from absolute PL imaging as a function atomic ratio [CsI]/[PbI_2]. The Shockley-Queisser limit calculated for each position is also shown as a reference. **(b)** Diffusion length (L_d) as a function of atomic ratio [CsI]/[PbI_2]. The dotted grey line shows the thickness of the $CsPbI_3$ film.

The optoelectronic properties reported in the previous section can be combined to assess the charge carrier transport and recombination parameters that are directly relevant to the performance and operation of solar cells based on the investigated materials. To estimate the implied open-circuit voltage (iV_{oc}) of the γ-phase, we calculated the quasi-Fermi level splitting (QFLS) from the photoluminescence data at 300 K as a function of position on the sample (***Figure 3a***). The values were obtained from the calibrated PL spectra at each position in a similar way as reported previously for mixed cation, mixed halide organic-inorganic perovskites.[45,46] QFLS values between 1.14 and 1.24 ±0.02 eV are obtained, corresponding to the maximum achievable open circuit voltage (iV_{oc}) that a given absorber layer could generate in a solar cell, assuming that the charge transport and contact layers do not alter the recombination at the perovskite surface. Figure 3a shows both the QFLS values in the radiative Shockley Queisser limit and the QFLS measured on the $CsPbI_3$ films (iV_{oc}), where the distance between both values indicates the non-radiative recombination losses in the material. It can be seen that as the [CsI]/[PbI_2] ratio increases the non-radiative recombination losses are reduced and the iV_{oc} values become larger.

These iV_{oc} values correspond to an EQE_{PL} of approximately ~0.01 % (***Figure 2d***), which is around two orders of magnitude below the EQE_{PL} reported previously for state-of-the-art bare mixed cation, mixed halide organic-inorganic perovskite films, and similar to the EQE_{PL} measured in ~20 % efficient full stack solar cells.[45,47] This indicates that non-radiative recombination in these inorganic perovskites is still larger than in the mixed cation, mixed halide organic-inorganic perovskites absorber layers used to fabricate high efficiency solar cell devices. With the knowledge of the charge carrier mobilities and lifetimes the diffusion length $L_d = \sqrt{\tau_{SRH}\ \mu\ k_B T/q}$ can be estimated for the investigated films assuming balanced electron and hole mobilities $\mu_n = \mu_p$ for the sum mobilities derived from OPTP, as the effective

masses of electrons and holes are very similar.[48] As can be seen in ***Figure 3b***, the diffusion length is found to be larger than 2 μm for most of the compositional region of the brown phase, except close to the phase boundary, where rapidly decreasing values are derived. We note that the maximum diffusion length observed is about four times larger than the thickness of the film (~450 nm) (see ***Figure 3b***), which clearly shows that the CsI-rich γ-phase investigated in this study is well suited for the fabrication of solar cells.

2.3 Photovoltaic performance.

P-i-n type (so called "inverted") solar cells were made employing poly(triarylamine) (PTAA) as a hole transporting material and fullerene C_{60} as electron transport layer (***Figure 4a***). The current density - voltage (JV) scan of the best performing device is shown in ***Figure 4b***. Here we achieve a V_{OC} of 0.96 V, a short-circuit current density (J_{SC}) of 17.8 mA/cm^2, a fill factor *(FF)* of 73 % and a power conversion efficiency *(PCE)* of above 12 % in the reverse scan. We note that no significant differences are observed in the *JV* scans as function of scan speed or light soaking (see ***Figure S7***). The stabilized efficiency measured over three minutes by maximum power point (mpp) tracking shows a sharp drop within the first seconds before the *PCE* settles at 10.7 % (see **Figure *4c***). It is worth noting that the stabilized *PCE* is improved to 11.3 % within the first days after preparation and maintains this performance for several weeks which corresponds to a shelf life stability of over 1200 h (see inset in ***Figure 4c***). The current density measured in the *JV* scan matches quite well with the integrated current density from external quantum efficiency (*EQE*) of 17.3 mA/cm^2 shown in ***Figure 4d***. The cell shows an *EQE* of over 80 % over a wide range of the visible spectrum as a consequence of the large L_d values estimated from the TRPL and OPTP data. The drastic loss in measured V_{OC} in the *JV* scan compared to the iV_{oc} measured on the bare $CsPbI_3$

absorbers, as well as the strong hysteresis, may indicate a misaligned band structure due to non-optimal contact layers or severe interface recombination limiting the device performance. Therefore, optimizing the contact layers is the most promising approach to further increase the efficiency of the presented $CsPbI_3$ solar cell.

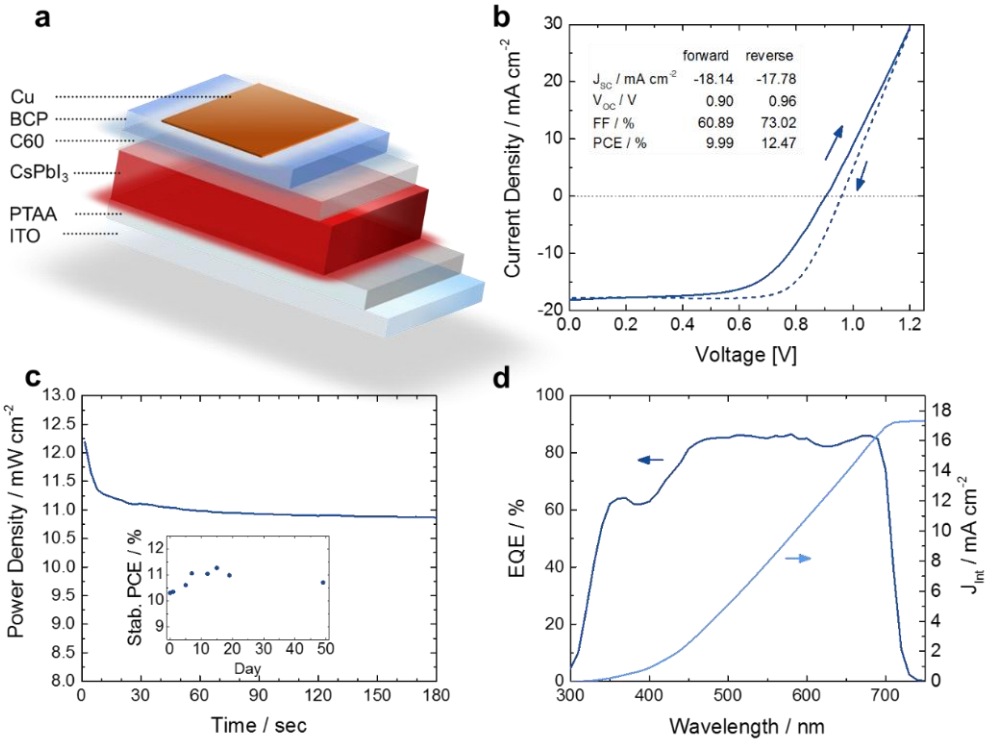

Figure 4 (a) Schematic of the p-i-n type device configuration used in this work. **(b)** JV scan of the best performing device measured at day 15 after preparation with a scan rate of 250 mV/s. A strong hysteresis effect between forward and reverse scan is observed as indicated. **(c)** Power conversion efficiency of the same device over time by maximum power point tracking over 3 minutes. The inset shows the stabilized power conversion efficiency after 3 minutes maximum power point tracking over the course of several weeks. **(d)** External quantum efficiency (EQE) spectra under 1 sun AM1.5G illumination on the left axis. Integrated photocurrent density from EQE spectra on the right axis.

3. Conclusions

In conclusion we have shown that inorganic $CsPbI_3$ can be directly synthesized in the perovskite sγ−phase at low temperature by co-evaporation under CsI-rich composition. Direct correspondence between the different polymorphs and their compositional region of stability is obtained employing samples which exhibit a linear gradient in the $[CsI]/[PbI_2]$ ratio. Lack of detectable secondary phases in the CsI-rich regime indicates the presence of a hollow perovskite structure with Schottky defect pairs. Optoelectronic analysis shows promising charge transport and recombination properties with electron and hole sum mobilities above 60 cm^2/Vs and carrier lifetimes larger than 70 ns, resulting in large diffusion lengths > 2 μm and an implied V_{oc} of up to 1.24 eV. P-i-n type solar cells fabricated with the γ-$CsPbI_3$ phase obtained by co-evaporation show stabilized efficiencies over 11 % and very high shelf stability of over 1200 h. Since the V_{OC} values of these solar cells are currently about 300 mV smaller than the implied V_{oc} measured for the bare absorber material, significant further improvements are expected from a further optimization/exploration of the charge transport and contact layers in these solar cells.

4. Experimental Section

Film preparation:

Quartz glass substrates were transferred into the vacuum chamber from inside a N_2 filled glove box. The chamber was pumped down to a pressure of ~10^{-7} hPa. CsI and PbI_2 (both Sigma Aldrich, purity: 99.999% trace metals basis) were thermally co-evaporated at 460 °C and 230 °C, respectively. The evaporation rate of the PbI_2 source was kept constant at 1 $nmol/(cm^2 \cdot 10s)$. The rate of the CsI source was adjusted to result in the molar ratios as stated in the text. The temperature of the substrate was kept constant at 50 °C during the entire evaporation by a PID controlled contact heater.

Cell fabrication and characterization:

Patterned indium tin oxide (ITO) glass substrates (25x25 mm^2, 15 Ω sq^{-1}, patterned by Automatic Research GmbH) were cleaned sequentially for 15 min with a 2 % Mucasol solution in water (Schülke), water, Acetone and Isopropanol in an ultrasonic bath. Subsequently, the substrates were treated in an UV-ozone cleaner for 15 min, before spin-coating a 2 mg/ml solution of poly(triaryl amine) (PTAA) in Toulene at 4000 rpm for 35 s (5 s acceleration) onto the substrates. The PTAA-coated substrates were heated at 100 °C for 10 min on a hotplate. Then, they were transferred to the perovskite evaporation chamber and ~500 nm of CsI and PbI_2 were evaporated at a nominal molar ratio of 1.2:1 as described above. The cells were completed by evaporation of 23 nm C_{60}, 8 nm BCP and 100 nm Cu-contacts at a base pressure of under 1E-6 mbar with evaporation rates of ca. 0.1-0.4 Å/s. The active solar cell area is defined by the overlap of the Cu stripe and the underlying ITO (0.16 cm^2).

JV Scan and EQE

Current-voltage characteristics under 1 sun equivalent illumination were recorded using an Oriel LCS-100 class ABB solar simulator in a N_2-filled glovebox and a Keithley 2400 Source Measure Unit. The voltage was swept in 20 mV steps with an integration time of 40 ms per point and settling time of 40 mV after voltage application, corresponding to a scan speed of 250 mV/s.

EQE spectra were recorded with an Oriel Instruments QEPVSI-b system with a Newport 300 W xenon arc lamp, controlled by TracQ-Basic software. The white light is split into monochromatic light by a Newport Cornerstone 260 monochromator and chopped at a frequency of 78 Hz before being conducted to the PSC surface via optical fibers. The system is calibrated using a Si reference cell with known spectral response before every measurement and cross-checked with an EQE system at the facilities of the Competence Centre Thin-Film- and Nanotechnology for Photovoltaics Berlin (PVcomB). The electrical response of the

device under test is measured with a Stanford Research SR830 Lock-In amplifier and evaluated in TracQ.

XRD mapping:

The XRD mapping was performed at the BL-10 of DELTA synchrotron in Dortmund, Germany. For easy comparison with common measurements with a Cu-tube the energy was selected to be monochromatic 8.05 keV. The incident angle was kept constant at 5°. The footprint on the sample was adjusted by slits to be 3 mm by 3 mm. The data was taken with a PILATUS 100K 2D detector. The diffraction patterns were obtained by integrating over the entire visible section of the diffraction ring.

Reference measurements were taken at a Panalytical X'Pert diffractometer with a Cu-tube.

XRF mapping:

XRF mapping was performed using a Bruker M4 Tornado with a Rh-tube and a poly-capillary optic with a spot size of 20 μm. The quantification was performed by employing the binary components as reference standards.

Absolute intensity PL hyperspectral imaging:

The sample was sealed between to quartz glasses to perform these measurements. Absolute photoluminescence was performed by excitation with two 450 nm LEDs equipped with diffuser lenses. The intensity of the LEDs was 1.6 x 1021 photons m^{-2} s^{-1}. The photoluminescence detection was performed with a CCD camera coupled with a liquid crystal tuneable filter. The system was calibrated to absolute photon numbers.

THz-mobility scan:

The mobility was measured by time resolved terahertz spectroscopy based on an amplified TiSa-laser system. To this end, charge carriers were photo-excited by a 400 nm pump pulse with a repetition rate of 150 kHz, and a power density of 46 mW/cm^2. The induced change in transmission of a terahertz probe pulse was measured by electro-optical sampling in a ZnTe crystal. This change was modelled numerically by the transfer matrix method which yields the

sum mobility of excited electrons and holes. The mobility scan was performed at the maximum of the THz pulse.

Time resolved photoluminescence:

TRPL measurements were performed at an excitation wavelength of 670 nm (≤ 3nm bandwidth) using a pulsed laser source at 608 kHz repetition. The incident photon flux has Gaussian time dependence with pulse length ≤ 60 ps. An excitation spot with Gaussian profile of diameter 30 µm was used at 3 µW excitation power. Time-correlated single photon counting was used for detection with an InGaAs photomultiplier with an instrument response function less than 250 ps. PL emission from the samples was taken panchromatically. TRPL line-scan data was acquired every 1 mm across the device. The data is fitted by the decay rate in low injection, where the carriers decay proportional to Δn.

Acknowledgements

The spatially resolved X-ray diffraction experiments were performed at Beamline BL10 at the DELTA Synchrotron Radiation Facility, Dortmund, Germany. We gratefully acknowledge Dirk Lützenkirchen-Hecht and Ralph Wagner for technical advice and consultation with data analysis as well as the DELTA machine group for providing synchrotron radiation reliably. The authors acknowledge financial support from the HyPerCells joint Graduate School (www.perovskites.de). A.A.A., M.J. and S.A. are funded by the German Federal Ministry of Education and Research (BMBF), within the project "Materialforschung für die Energiewende" (grant no. 03SF0540). S.A. further acknowledges funding by the German Federal Ministry for Economic Affairs and Energy (BMWi) through the "PersiST" project (grant no. 0324037C).

References

[1] N. J. Jeon, H. Na, E. H. Jung, T. Y. Yang, Y. G. Lee, G. Kim, H. W. Shin, S. Il Seok, J. Lee, J. Seo, *Nat. Energy* **2018**, *3*, 1.

[2] M. A. Green, Y. Hishikawa, E. D. Dunlop, D. H. Levi, J. Hohl-Ebinger, A. W. Y. Ho-Baillie, *Prog. Photovoltaics Res. Appl.* **2018**, *26*, 3.

[3] G. E. Eperon, G. M. Paternò, R. J. Sutton, A. Zampetti, A. A. Haghighirad, F. Cacialli, H. J. Snaith, *J. Mater. Chem. A* **2015**, *3*, 19688.

[4] M. Kulbak, S. Gupta, N. Kedem, I. Levine, T. Bendikov, G. Hodes, D. Cahen, *J. Phys.*

Chem. Lett. **2016**, *7*, 167.
[5] M. Kulbak, D. Cahen, G. Hodes, *J. Phys. Chem. Lett.* **2015**, *6*, 2452.
[6] C. C. Stoumpos, C. D. Malliakas, J. A. Peters, Z. Liu, M. Sebastian, J. Im, T. C. Chasapis, A. C. Wibowo, D. Y. Chung, A. J. Freeman, B. W. Wessels, M. G. Kanatzidis, *Cryst. Growth Des.* **2013**, *13*, 2722.
[7] W. Ahmad, J. Khan, G. Niu, J. Tang, *Sol. RRL* **2017**, *1*, 1700048.
[8] Y. Wang, T. Zhang, M. Kan, Y. Zhao, *J. Am. Chem. Soc.* **2018**, *140*, 12345.
[9] E. M. Sanehira, A. R. Marshall, J. A. Christians, S. P. Harvey, P. N. Ciesielski, L. M. Wheeler, P. Schulz, L. Y. Lin, M. C. Beard, J. M. Luther, *Sci. Adv.* **2017**, *3*, eaao4204.
[10] A. Marronnier, G. Roma, S. Boyer-Richard, L. Pedesseau, J. M. Jancu, Y. Bonnassieux, C. Katan, C. C. Stoumpos, M. G. Kanatzidis, J. Even, *ACS Nano* **2018**, *12*, 3477.
[11] C. C. Stoumpos, C. D. Malliakas, M. G. Kanatzidis, *Inorg. Chem.* **2013**, *52*, 9019.
[12] Y. Hu, F. Bai, X. Liu, Q. Ji, X. Miao, T. Qiu, S. Zhang, *ACS Energy Lett.* **2017**, *2*, 2219.
[13] A. Swarnkar, A. R. Marshall, E. M. Sanehira, B. D. Chernomordik, D. T. Moore, J. A. Christians, T. Chakrabarti, J. M. Luther, *Science (80-.).* **2016**, *354*, 92.
[14] R. J. Sutton, G. E. Eperon, L. Miranda, E. S. Parrott, B. A. Kamino, J. B. Patel, M. T. Hörantner, M. B. Johnston, A. A. Haghighirad, D. T. Moore, H. J. Snaith, *Adv. Energy Mater.* **2016**, *6*, 1502458.
[15] P. Pistor, T. Burwig, W. Fra, **2018**, *3*, DOI 10.1021/acs.jpclett.8b02059.
[16] L. A. Frolova, D. V. Anokhin, A. A. Piryazev, S. Y. Luchkin, N. N. Dremova, K. J. Stevenson, P. A. Troshin, *J. Phys. Chem. Lett.* **2017**, *8*, 67.
[17] E. M. Hutter, R. J. Sutton, S. Chandrashekar, M. Abdi-Jalebi, S. D. Stranks, H. J. Snaith, T. J. Savenije, *ACS Energy Lett.* **2017**, *2*, 1901.
[18] C.-Y. Chen, H.-Y. Lin, K.-M. Chiang, W.-L. Tsai, Y.-C. Huang, C.-S. Tsao, H.-W. Lin, *Adv. Mater.* **2017**, *29*, 1605290.
[19] Y. El Ajjouri, F. Palazon, M. Sessolo, H. J. Bolink, *Chem. Mater.* **2018**, *30*, 7423.
[20] Q. Ma, S. Huang, S. Chen, M. Zhang, C. F. J. Lau, M. N. Lockrey, H. K. Mulmudi, Y. Shan, J. Yao, J. Zheng, X. Deng, K. Catchpole, M. A. Green, A. W. Y. Ho-Baillie, *J. Phys. Chem. C* **2017**, *121*, 19642.
[21] Q. Ma, S. Huang, X. Wen, M. A. Green, A. W. Y. Ho-Baillie, *Adv. Energy Mater.* **2016**, *6*, 1502202.
[22] Z. Li, J. Xu, S. Zhou, B. Zhang, X. Liu, S. Dai, J. Yao, *ACS Appl. Mater. Interfaces* **2018**, *10*, 38183.
[23] H. Chen, S. Xiang, W. Li, H. Liu, L. Zhu, S. Yang, *Sol. RRL* **2018**, *2*, 1700188.
[24] R. E. Beal, D. J. Slotcavage, T. Leijtens, A. R. Bowring, R. A. Belisle, W. H. Nguyen, G. F. Burkhard, E. T. Hoke, M. D. McGehee, *J. Phys. Chem. Lett.* **2016**, *7*, 746.
[25] C. F. J. Lau, M. Zhang, X. Deng, J. Zheng, J. Bing, Q. Ma, J. Kim, L. Hu, M. A. Green, S. Huang, A. Ho-Baillie, *ACS Energy Lett.* **2017**, *2*, 2319.
[26] Q. Wang, X. Zheng, Y. Deng, J. Zhao, Z. Chen, J. Huang, *Joule* **2017**, *1*, 371.
[27] G. E. Eperon, G. M. Paternò, R. J. Sutton, A. Zampetti, A. A. Haghighirad, F. Cacialli, H. J. Snaith, *J. Mater. Chem. A* **2015**, *3*, 19688.
[28] T. Zhang, M. I. Dar, G. Li, F. Xu, N. Guo, M. Grätzel, Y. Zhao, *Sci. Adv.* **2017**, *3*, e1700841.
[29] F. Li, Y. Pei, F. Xiao, T. Zeng, Z. Yang, J. Xu, J. Sun, B. Peng, M. Liu, *Nanoscale* **2018**, *10*, 6318.
[30] Y. Jiang, J. Yuan, Y. Ni, J. Yang, Y. Wang, T. Jiu, M. Yuan, J. Chen, *Joule* **2018**, DOI 10.1016/j.joule.2018.05.004.
[31] *ACS Nano* **2017**, *11*, 3819.
[32] R. J. Sutton, M. R. Filip, A. A. Haghighirad, N. Sakai, B. Wenger, F. Giustino, H. J.

Snaith, *ACS Energy Lett.* **2018**, *3*, 1787.
[33] S. Dastidar, C. J. Hawley, A. D. Dillon, A. D. Gutierrez-Perez, J. E. Spanier, A. T. Fafarman, *J. Phys. Chem. Lett.* **2017**, *8*, 1278.
[34] A. Walsh, D. O. Scanlon, S. Chen, X. G. Gong, S. H. Wei, *Angew. Chemie - Int. Ed.* **2015**, *54*, 1791.
[35] I. Spanopoulos, W. Ke, C. C. Stoumpos, E. C. Schueller, O. Y. Kontsevoi, R. Seshadri, M. G. Kanatzidis, **2018**, DOI 10.1021/jacs.8b01034.
[36] B. Zhao, S.-F. Jin, S. Huang, N. Liu, J.-Y. Ma, D.-J. Xue, Q. Han, J. Ding, Q.-Q. Ge, Y. Feng, J.-S. Hu, *J. Am. Chem. Soc.* **2018**, *140*, 11716.
[37] P. U. Jepsen, D. G. Cooke, M. Koch, *Laser Photon. Rev.* **2011**, *5*, 124.
[38] H. Hempel, A. Redinger, I. Repins, C. Moisan, G. Larramona, G. Dennler, M. Handwerg, S. F. Fischer, R. Eichberger, T. Unold, *J. Appl. Phys.* **2016**, *120*, DOI 10.1063/1.4965868.
[39] S. Dastidar, S. Li, S. Y. Smolin, J. B. Baxter, A. T. Fafarman, *ACS Energy Lett.* **2017**, *2*, 2239.
[40] F. Staub, H. Hempel, J. C. Hebig, J. Mock, U. W. Paetzold, U. Rau, T. Unold, T. Kirchartz, *Phys. Rev. Appl.* **2016**, *6*, 044017.
[41] Z. Xiao, Y. Yan, *Adv. Energy Mater.* **2017**, *7*, 1701136.
[42] Z. Xiao, W. Meng, J. Wang, D. B. Mitzi, Y. Yan, *Mater. Horizons* **2017**, *4*, 206.
[43] Y. G. Kim, T.-Y. Kim, J. H. Oh, K. S. Choi, Y.-J. Kim, S. Y. Kim, *Phys. Chem. Chem. Phys.* **2017**, *19*, 6257.
[44] T. S. Ripolles, K. Nishinaka, Y. Ogomi, Y. Miyata, S. Hayase, *Sol. Energy Mater. Sol. Cells* **2016**, *144*, 532.
[45] M. Stolterfoht, C. M. Wolff, J. A. Márquez, S. Zhang, C. J. Hages, D. Rothhardt, S. Albrecht, P. L. Burn, P. Meredith, T. Unold, D. Neher, *Nat. Energy* **2018**, DOI 10.1038/s41560-018-0219-8.
[46] R. T. Ross, *J. Chem. Phys.* **1967**, *46*, 4590.
[47] Z. Liu, L. Krückemeier, B. Krogmeier, B. Klingebiel, J. A. Márquez, S. Levcenko, S. Öz, S. Mathur, U. Rau, T. Unold, T. Kirchartz, *ACS Energy Lett.* **2018**, 110.
[48] M. Afsari, A. Boochani, M. Hantezadeh, *Optik (Stuttg).* **2016**, *127*, 11433.

Supporting Information

Low temperature synthesis of stable γ-$CsPbI_3$ perovskite layers for solar cells

Pascal Becker[1,2], José A. Márquez[1], Justus Just[1,3], Amran Al-Ashouri[4], Charles Hages[1], Hannes Hempel[1], Marko Jošt[4], Steve Albrecht[4], Ronald Frahm[2] and Thomas Unold[1]*

[1]Helmholtz-Zentrum-Berlin, Hahn-Meitner-Platz 1, 14109 Berlin, Germany
[2]Bergische Universitaet Wuppertal, Gausstrasse 20, 42119 Wuppertal, Germany
[3]Lund University, Paradisgatan 2, 22100 Lund, Sweden
[4]Young Investigator Group Perovskite Tandem Solar Cells, Helmholtz-Zentrum-Berlin, Hahn Meitner-Platz 1, 14109 Berlin, Germany

***Table S1**. Comparison of calculated lattice parameters obtained for the γ-phase in this work and the values in literature.*

	a / Å	b / Å	c / Å	a / b	c/(a+b)	V / Å^3	T / K
Marronnier et al. [1]	8.620	8.852	12.501	0.9738	0.7155	953.9	325
Sutton et al. [2]	8.577	8.856	12.472	0.9684	0.7154	947.3	293
Bertolotti NCs [3]	8.612	8.845	12.524	0.9737	0.7174	954.1	298
This work	8.629	8.834	12.477	0.9768	0.7145	951.1	~298

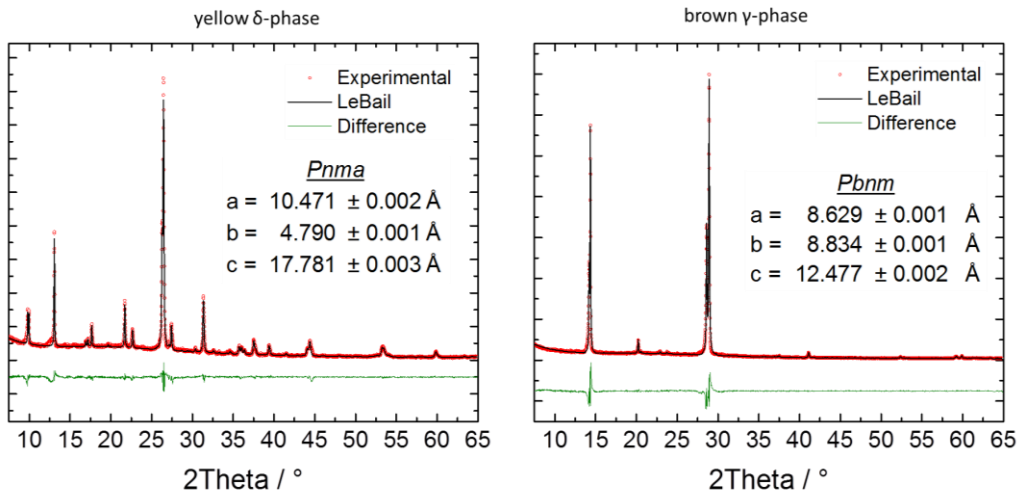

Figure S1 XRD patterns were measured in the brown and yellow regions of the sample with a Panalytical X'Pert diffractometer measured in Bragg-Brentano-geometry with a Cu K-alpha X-ray tube. Lattice parameters are determined by Le Bail refinement.

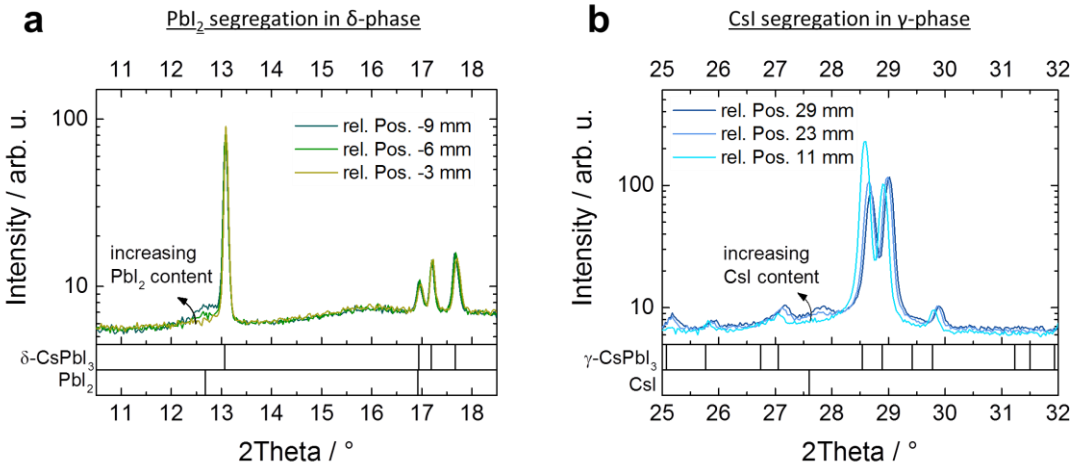

Figure S2 (a) Synchrotron measured XRD pattern showing PbI_2 segregation with increasing PbI_2 content in the film as well as **(b)** CsI segregation with increasing CsI content in the film. The bars below the measurements correspond to expected peak positions for the respective compound from non-refined theoretical models. The shift to higher angles in **(b)** is due to a small tilt of the sample while performing the line-scan. We note that other ternary compounds like Cs_4PbI_6 present numerous reflections between 25° and 30°. This does not allow us to ambiguously discard small amounts of this phase which cannot be resolved taking into account the detection limits of our measurements.

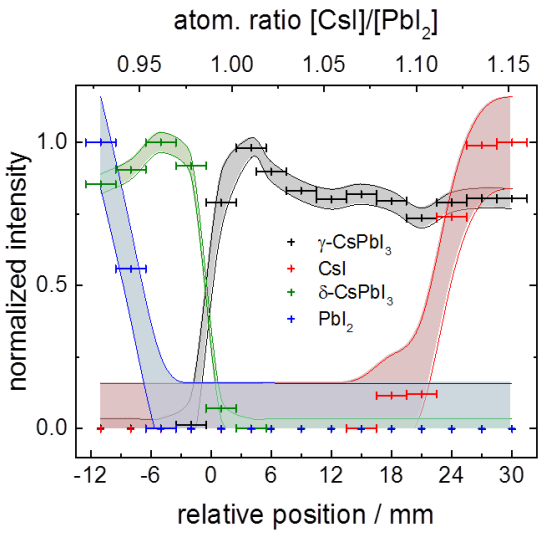

Figure S3 Normalized XRD intensity of the different phases in the $CsPbI_3$ film dependent on the position and [CsI]/[PbI_2] atomic ratio. The intensities were obtained by fitting a Gaussian to individual peaks of the respective phase and integration of the area. To avoid influences from changing texture, multiple peaks from different orientations were averaged. The four components were normalized individually to their maximum intensity within the line scan.

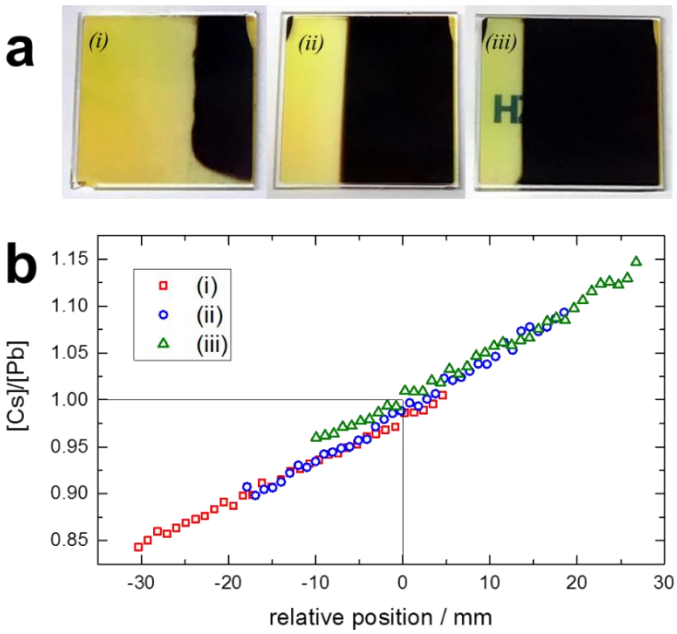

Figure S4 Dependence of the composition on the position relative to the boundary between yellow δ-phase and brown γ-phase. **(a)** Images of the as-evaporated samples with ratio of evaporation rates [CsI]:[PbI_2] of (i) 0.94:1, (ii) 0.99:1 and (iii) 1.10:1. **(b)** Composition of the sample taken by XRF. The [Cs]/[Pb] ratio is plotted over the position relative to the phase boundary.

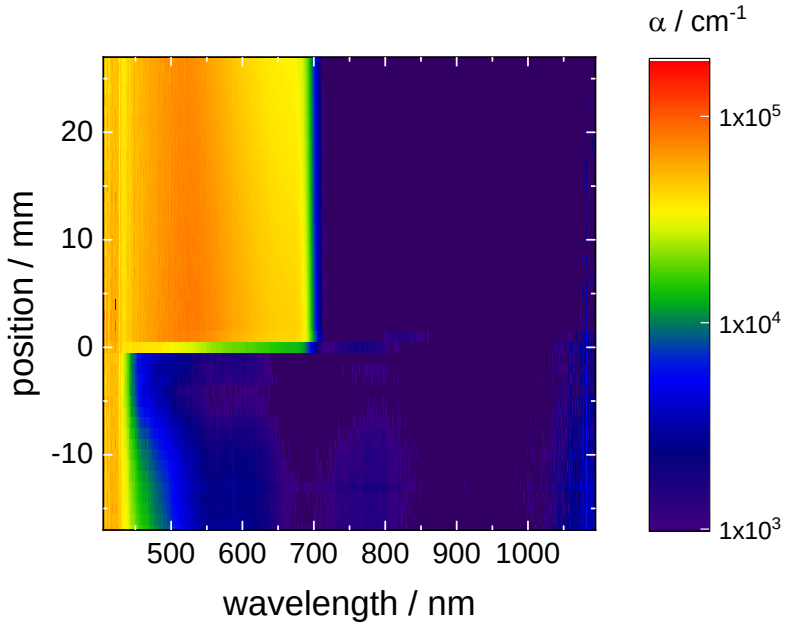

Figure S5 Absorption coefficient as a function of position on the sample.

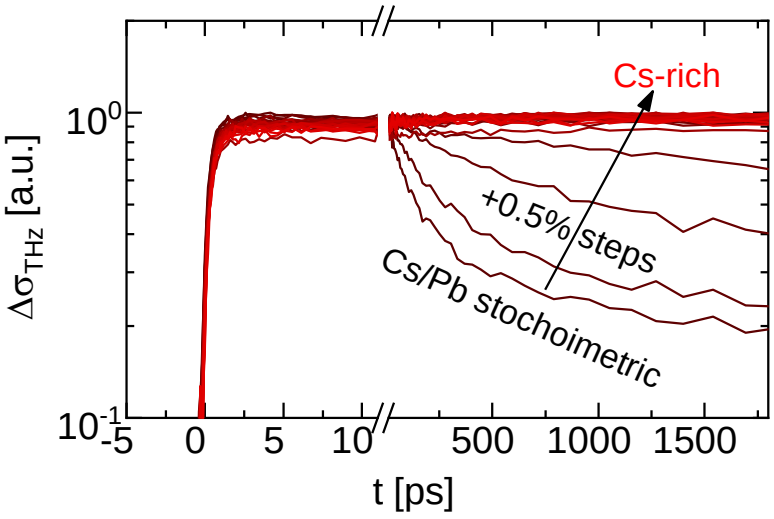

Figure S6 OPTP transients for different compositions in Figure 2c. It can be seen that for Cs/Pb ratios approaching stochiometry (from the Cs-rich side) the photoconductivity transients become shorter with decay times <1ns for the stoichometric case.

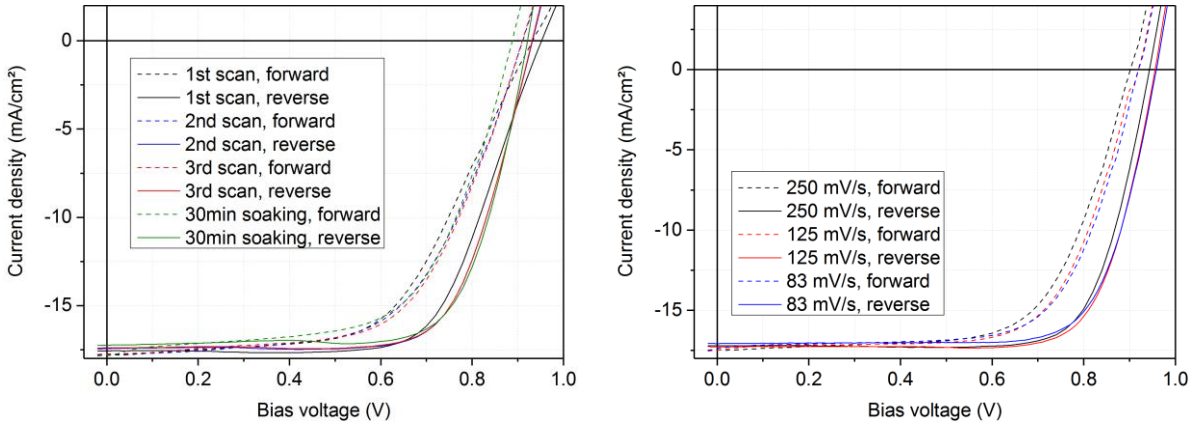

Figure S7 Repeated JV curves under simulated 1-sun equivalent AM1.5g illumination. Left: Three subsequent scans and one additional scan after 30 mins of light soaking in 1-sun equivalent illumination in a non-cooled substrate holder show the high stability and repeatability of the fabricated solar cells under repeated measurement. Right: In contrast to the behavior of solution-processed mixed cation/mixed halide perovskite solar cells, the hysteresis index does not significantly change for different scan speeds for our cells.

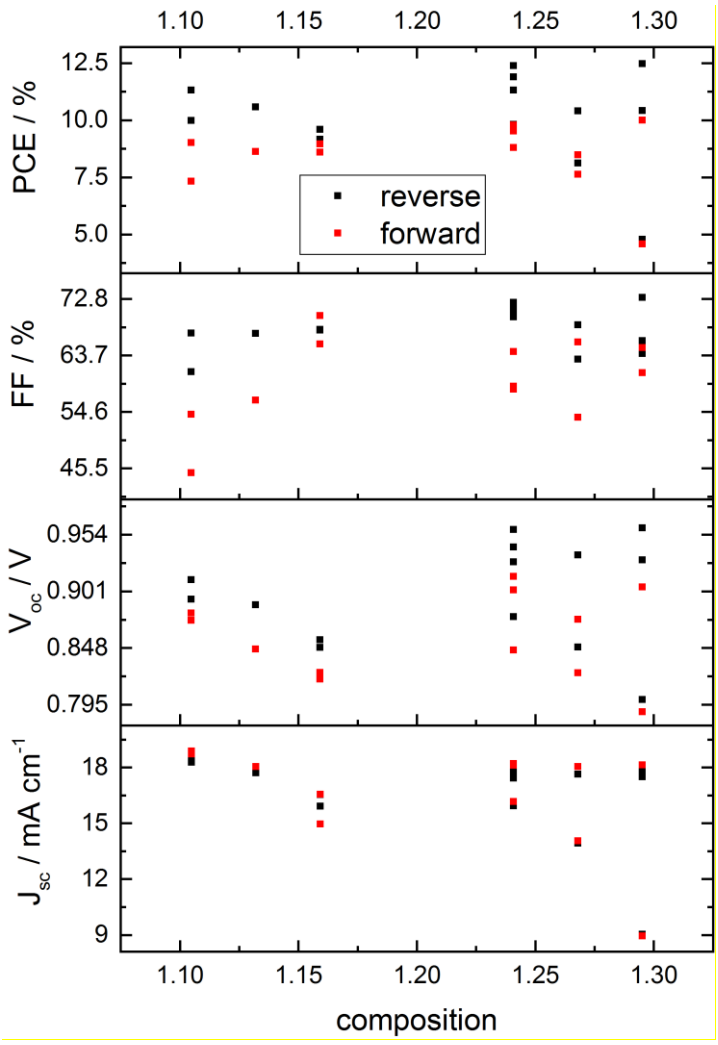

Figure S8 Statistics of solar cell performance parameters for cells fabricated with different chemical compositions of the $CsPbI_3$-absorber.

(1) A. Marronnier, G. Roma, S. Boyer-Richard, L. Pedesseau, J.M. Jancu, Y. Bonnassieux, C. Katan, C.C. Stoumpos, M. G. Kanatzidis, J. Even, *ACS Nano* **2018**, *12* (4), 3477–3486.

(2) R. J. Sutton, M.R. Filip, A. A. Haghighirad,N. Sakai, B. Wenger, F. Giustino, H. J. Snaith, Cubic or Orthorhombic? Revealing the Crystal Structure of Metastable Black-Phase CsPbI 3 by Theory and Experiment. *ACS Energy Lett.* **2018**, *3* (8), 1787–1794..

(3) F. Bertolotti, L. Protesescu, M. V. Kovalenko, S. Yakunin, A. Cervellino, S. J. L. Billinge, M. W. Terban, J. S. Pedersen, N. Masciocchi, A. Guagliardi, *ACS Nano* **2017**, *11*, 3819–3831.